Supplement of Atmos. Chem. Phys., 26, 851–867, 2026
https://doi.org/10.5194/acp-26-851-2026-supplement


Atmospheric Chemistry and Physics
Open Access

*Supplement of*

# Tracking surface ozone responses to clean air actions under a warming climate in China using machine learning

**Jie Fang et al.**

*Correspondence to:* Yunjiang Zhang (yjzhang@nuist.edu.cn)

## Supporting Text

### S1. Ozone sensitivity diagnosis with FNR

Ozone concentrations show a significant nonlinear relationship with their precursors, which can be classified into three types: the VOC-limited regime, the $NO_x$-limited regime, and translational. The ratio of HCHO to $NO_2$ (FNR) serves as a reactive weighting of VOC/$NO_x$ and is one of the diagnostic indicators of ozone-sensitive intervals (Sillman, 1995), this is particularly suited to the analysis of satellite data and has been widely used in related research (Jin et al., 2020; Jin and Holloway, 2015; Wang et al., 2021). Based on the framework described by Ren et al. (2022) and Jin et al. (2015), we developed a diagnostic approach better suited to our dataset, and this study on ozone sensitivity diagnosis for the summer periods of 2018-2023 is based on the following criteria:

$$FNRavg < 3.0 \, and \, FNRavg + FNRsd < 4.0 : \mathrm{VOC-limited}$$

$$FNRavg > 3.0 \, and \, FNRavg - FNRsd > 2.0 : \mathrm{NO_x-limited}$$

$$Otherwise: translational$$

where $FNRavg$ and $FNRsd$ denote the time-mean and standard deviation of the FNR for the target time period.

### S2. Uncertainty analysis for the FEA method

To assess the uncertainty associated with the FEA method, we applied a cross-matrix validation approach, training models for each year as the baseline year (i.e., using each year as a reference for emissions) to calculate the relative contribution of anthropogenic emissions in different years. Specifically, we alternated the role of each year as the model training year (i.e., the fixed emission reference year) and the prediction year. As illustrated in Eqs. S1 and S2, for any two years, *n* and *m*, can both serve as either the model training year or the model prediction year. For instance, $\Delta ANT_{n(m)}$ represents the scenario where year *n* is used as the model training year and year *m* as the model prediction year, while $\Delta ANT_{m(n)}$ denotes the reverse, with year *m* as the model training year and year *n* as the model prediction year.

$$\Delta ANT_{n(m)} = OBS_m - Pred_{n(m)} - RES_n \tag{S1}$$

$$\Delta ANT_{m(n)} = OBS_n - Pred_{m(n)} - RES_m \tag{S2}$$

From Eq. (S1), the observed data for year m ($OBS_m$) can be expressed as the sum of $Pred_{n(m)}$, $RES_n$, and $\Delta ANT_{n(m)}$. Theoretically, if there were no uncertainty in the use of data from different years for model training, then $\Delta ANT_{n(m)} = -\Delta ANT_{m(n)}$. Therefore, the uncertainty $u_{n(m)}$ associated with the FEA method can be represented by Eq. S3:

$$u_{n(m)} = \frac{(Pred_{n(m)}+RES_n-(OBS_n-Pred_{m(n)}-RES_m))-OBS_m}{OBS_m} \tag{S3}$$

**S3. COVID-19 lockdown-driven computation based on the FEA method**

Wuhan, where the outbreak of the virus was first detected, issued a lockdown policy on January 23, 2020, followed by outbreaks in other Chinese cities within the next few days. A strict national quarantine lasting one to two months was then imposed. Most Chinese cities gradually relaxed their quarantine measures starting in April, and Wuhan reopened on April 8th. Therefore, we consider the first four months of 2020 as the COVID-19 Lockdown period (LD) by referring to the definition of COVID-19 lockdown by Geng et al. (2024). The difference between the observed MDA8 ozone concentration in LD ($Obs_{LD}$) and the corresponding model prediction ($Pred_{(i,LD)}$) is scaled by the ratio of the samples in LD ($n_{LD}$) to the total number of samples in 2020 ($n_{All}$) (i.e., $C_{LD} = n_{LD}/n_{All}$). This value represents the combined contribution of short-term unconventional emission reductions and long-term conventional emission control policies during the COVID-19 lockdown. The impact of long-term conventional emission reductions is estimated by the difference between observed and predicted MDA8 ozone concentrations during non-blockade periods ($Obs_{NLD} - Pred_{(i,NLD)}$), scaled by $C_{LD}$. Thus, the relative contribution of the COVID-19 lockdown to the MDA8 ozone trend（$COVID_{(i,LD)}$）can be calculated by Eq. S4:

$$COVID_{(i,LD)} = C_{LD} \times \left(OBS_{LD} - P_{(i,LD)}\right) - C_{LD} \times \left(OBS_{NLD} - P_{(i,NLD)}\right) \tag{S4}$$

**Supporting Tables**

**Table S1. Overview of the characteristics of the ERA5 variables used in the analysis of this study.**

| Abbreviations | Description |
|---|---|
| T2m | Temperature at 2m (K) |
| SR | Shortwave solar radiation ($W/m^2$) |
| SP | Sea level pressure (Pa) |
| BLH | Boundary layer height (m) |
| TP | Total precipitation (m) |
| RH | Surface relative humidity (%) |
| TCC | Total cloud cover |
| U10 | Zonal wind at 10m ($m\ s^{-1}$) |
| V10 | Meridional wind at 10m ($m\ s^{-1}$) |
| U850 | Zonal wind at 850 hPa ($m\ s^{-1}$) |
| V850 | Meridional wind at 850 hPa ($m\ s^{-1}$) |
| W850 | Vertical velocity at 850 hPa ($Pa\ s^{-1}$) |
| U650 | Zonal wind at 650 hPa ($m\ s^{-1}$) |
| V650 | Meridional wind at 650 hPa ($m\ s^{-1}$) |
| W650 | Vertical velocity at 650 hPa ($Pa\ s^{-1}$) |
| U500 | Zonal wind at 500 hPa ($m\ s^{-1}$) |
| V500 | Meridional wind at 500 hPa ($m\ s^{-1}$) |
| W500 | Vertical velocity at 500 hPa ($Pa\ s^{-1}$) |

**Table S2. Definitions of the 7 statistical indicators used in this study.**

| No. | Statistics (abbreviation) | Definition | Note |
|---|---|---|---|
| 1. | Mean Absolute Error (MAE) | $MAE = \frac{1}{n}\sum_{i=1}^{n}\lvert P_i - O_i \rvert$ | μg $m^{-3}$ |
| 2. | Root mean square error(RMSE) | $RMSE = \sqrt{\frac{\sum_{i=1}^{n}(P_i - O_i)^2}{n}}$ | μg $m^{-3}$ |
| 3. | Normalized Mean Squared Error(NMSE) | $NMSE = \frac{1}{n}\sum_{i=1}^{n}\frac{MSE}{VAR(P_i)}$ | Unitless, 0 ≤ NMSE ≤ 1 |
| 4. | Correlation coeffcient(R) | $R = \frac{\sum_{i=1}^{n}(O_i - \bar{O})(P_i - \bar{P})}{\sqrt{\sum_{i=1}^{n}(P_i - \bar{P})^2 \sum_{i=1}^{n}(O_i - \bar{O})^2}}$ | Unitless, -1 ≤ R ≤ 1 |
| 5. | Mean bias (MB) | $MB = \frac{1}{n}\sum_{i=1}^{n}(P_i - O_i)$ | μg $m^{-3}$ |
| 6. | Normalized mean bias(NMB) | $NMB = \frac{\sum_{i=1}^{n}(P_i - O_i)}{\sum_{i=1}^{n} O_i} \times 100$ | -100% ≤ NMB ≤ +∞ |
| 7. | Index of Agreement (IOA) | $IOA = 1 - \frac{\sum_{i=1}^{n}(P_i - O_i)^2}{\sum_{i=1}^{n}(\lvert P_i - \bar{O}\rvert + \lvert O_i - \bar{O}\rvert)^2}$ | Unitless, 0 ≤ IOA ≤ 1 |

**Table S3. Ten-fold cross-validation results of RF models for national input datasets.**

| $O_3$ | MAE | RMSE | NMSE | R | MB | NMB | IOA |
|---|---|---|---|---|---|---|---|
| 2015 | 13.8 | 20.9 | 0.06 | 0.88 | 0.07 | 21 | 0.93 |
| 2016 | 13.7 | 20.4 | 0.06 | 0.89 | 0.05 | 20 | 0.94 |
| 2017 | 14.3 | 21.3 | 0.05 | 0.90 | 0.06 | 19 | 0.95 |
| 2018 | 14.8 | 21.8 | 0.05 | 0.90 | 0.06 | 16 | 0.94 |
| 2019 | 14.1 | 20.7 | 0.05 | 0.90 | 0.02 | 17 | 0.94 |
| 2020 | 12.9 | 19.1 | 0.05 | 0.90 | 0.03 | 16 | 0.94 |
| 2021 | 13.2 | 19.2 | 0.05 | 0.90 | 0.01 | 15 | 0.94 |
| 2022 | 12.7 | 18.8 | 0.04 | 0.91 | -0.004 | 13 | 0.95 |
| 2023 | 13.0 | 18.8 | 0.04 | 0.91 | -0.02 | 12 | 0.95 |

**Table S4. Ten-fold cross-validation results of RF models for BTH input datasets.**

| $O_3$ | MAE | RMSE | NMSE | R | MB | NMB | IOA |
|---|---|---|---|---|---|---|---|
| 2015 | 14.9 | 19.9 | 0.04 | 0.93 | 0.01 | 17 | 0.96 |
| 2016 | 15.0 | 20.2 | 0.04 | 0.94 | 0.09 | 21 | 0.96 |
| 2017 | 16.2 | 21.5 | 0.03 | 0.94 | 0.02 | 17 | 0.97 |
| 2018 | 16.7 | 21.9 | 0.03 | 0.94 | 0.09 | 12 | 0.96 |
| 2019 | 15.3 | 20.2 | 0.03 | 0.94 | -0.04 | 12 | 0.97 |
| 2020 | 13.6 | 18.0 | 0.02 | 0.94 | -0.06 | 10 | 0.96 |
| 2021 | 14.0 | 18.4 | 0.03 | 0.94 | -0.02 | 11 | 0.96 |
| 2022 | 12.6 | 16.9 | 0.02 | 0.95 | -0.06 | 8 | 0.97 |
| 2023 | 12.7 | 16.9 | 0.02 | 0.95 | -0.12 | 6 | 0.97 |

**Table S5. Ten-fold cross-validation results of RF models for FWP input datasets.**

| $O_3$ | MAE | RMSE | NMSE | R | MB | NMB | IOA |
|---|---|---|---|---|---|---|---|
| 2015 | 11.6 | 15.7 | 0.03 | 0.94 | 0.04 | 13 | 0.96 |
| 2016 | 12.9 | 17.5 | 0.03 | 0.93 | 0.05 | 14 | 0.96 |
| 2017 | 14.8 | 19.8 | 0.03 | 0.95 | 0.07 | 14 | 0.97 |
| 2018 | 15.0 | 19.9 | 0.03 | 0.94 | 0.06 | 14 | 0.96 |
| 2019 | 13.8 | 18.2 | 0.03 | 0.95 | 0.12 | 15 | 0.97 |
| 2020 | 13.0 | 17.4 | 0.03 | 0.94 | -0.02 | 17 | 0.97 |
| 2021 | 14.1 | 18.8 | 0.03 | 0.94 | 0.04 | 14 | 0.96 |
| 2022 | 12.6 | 16.9 | 0.02 | 0.95 | -0.1 | 13 | 0.97 |
| 2023 | 12.4 | 16.6 | 0.02 | 0.95 | 0.02 | 10 | 0.97 |

**Table S6. Ten-fold cross-validation results of RF models for YRD input datasets.**

| $O_3$ | MAE | RMSE | NMSE | R | MB | NMB | IOA |
|---|---|---|---|---|---|---|---|
| 2015 | 17.2 | 26.6 | 0.09 | 0.85 | 0.11 | 27 | 0.91 |
| 2016 | 16.6 | 24.2 | 0.07 | 0.87 | 0.07 | 20 | 0.93 |
| 2017 | 17.0 | 24.5 | 0.06 | 0.89 | 0.06 | 20 | 0.94 |
| 2018 | 16.7 | 23.9 | 0.06 | 0.9 | 0.08 | 16 | 0.94 |
| 2019 | 16.3 | 22.7 | 0.05 | 0.9 | 0.09 | 18 | 0.94 |
| 2020 | 15.6 | 22.4 | 0.07 | 0.87 | 0.12 | 21 | 0.92 |
| 2021 | 14.9 | 21.5 | 0.06 | 0.9 | 0.02 | 16 | 0.94 |
| 2022 | 16.1 | 22.2 | 0.05 | 0.89 | 0.12 | 13 | 0.94 |
| 2023 | 15.7 | 21.8 | 0.05 | 0.9 | -0.04 | 15 | 0.94 |

**Table S7. Ten-fold cross-validation results of RF models for SCB input datasets.**

| $O_3$ | MAE | RMSE | NMSE | R | MB | NMB | IOA |
|---|---|---|---|---|---|---|---|
| 2015 | 21.8 | 31.2 | 0.14 | 0.72 | 0.06 | 39 | 0.83 |
| 2016 | 23.3 | 33.0 | 0.15 | 0.72 | 0.08 | 44 | 0.83 |
| 2017 | 24.3 | 34.1 | 0.15 | 0.72 | 0.04 | 48 | 0.83 |
| 2018 | 24.2 | 34.3 | 0.14 | 0.71 | 0.03 | 34 | 0.82 |
| 2019 | 23.4 | 33.2 | 0.15 | 0.72 | 0.05 | 37 | 0.83 |
| 2020 | 20.9 | 29.3 | 0.13 | 0.73 | 0.04 | 31 | 0.83 |
| 2021 | 20.7 | 29.0 | 0.11 | 0.75 | 0.07 | 26 | 0.85 |
| 2022 | 21.0 | 29.6 | 0.09 | 0.77 | 0.02 | 24 | 0.86 |
| 2023 | 20.8 | 29.3 | 0.10 | 0.75 | 0.01 | 21 | 0.85 |

**Table S8. Ten-fold cross-validation results of RF models for PRD input datasets.**

| $O_3$ | MAE | RMSE | NMSE | R | MB | NMB | IOA |
|---|---|---|---|---|---|---|---|
| 2015 | 9.3 | 14.5 | 0.05 | 0.94 | 0.11 | 17 | 0.96 |
| 2016 | 11.5 | 18.0 | 0.06 | 0.93 | 0.11 | 20 | 0.95 |
| 2017 | 9.6 | 16.1 | 0.07 | 0.93 | 0.06 | 21 | 0.96 |
| 2018 | 12.2 | 18.4 | 0.06 | 0.92 | 0.11 | 23 | 0.95 |
| 2019 | 10.8 | 16.3 | 0.06 | 0.93 | 0.07 | 21 | 0.95 |
| 2020 | 7.7 | 12.3 | 0.04 | 0.95 | -0.03 | 14 | 0.97 |
| 2021 | 9.8 | 14.8 | 0.05 | 0.93 | -0.004 | 14 | 0.96 |
| 2022 | 8.7 | 13.5 | 0.04 | 0.94 | 0.09 | 13 | 0.96 |
| 2023 | 9.5 | 14.0 | 0.05 | 0.93 | 0.05 | 14 | 0.96 |

## Supporting Figures

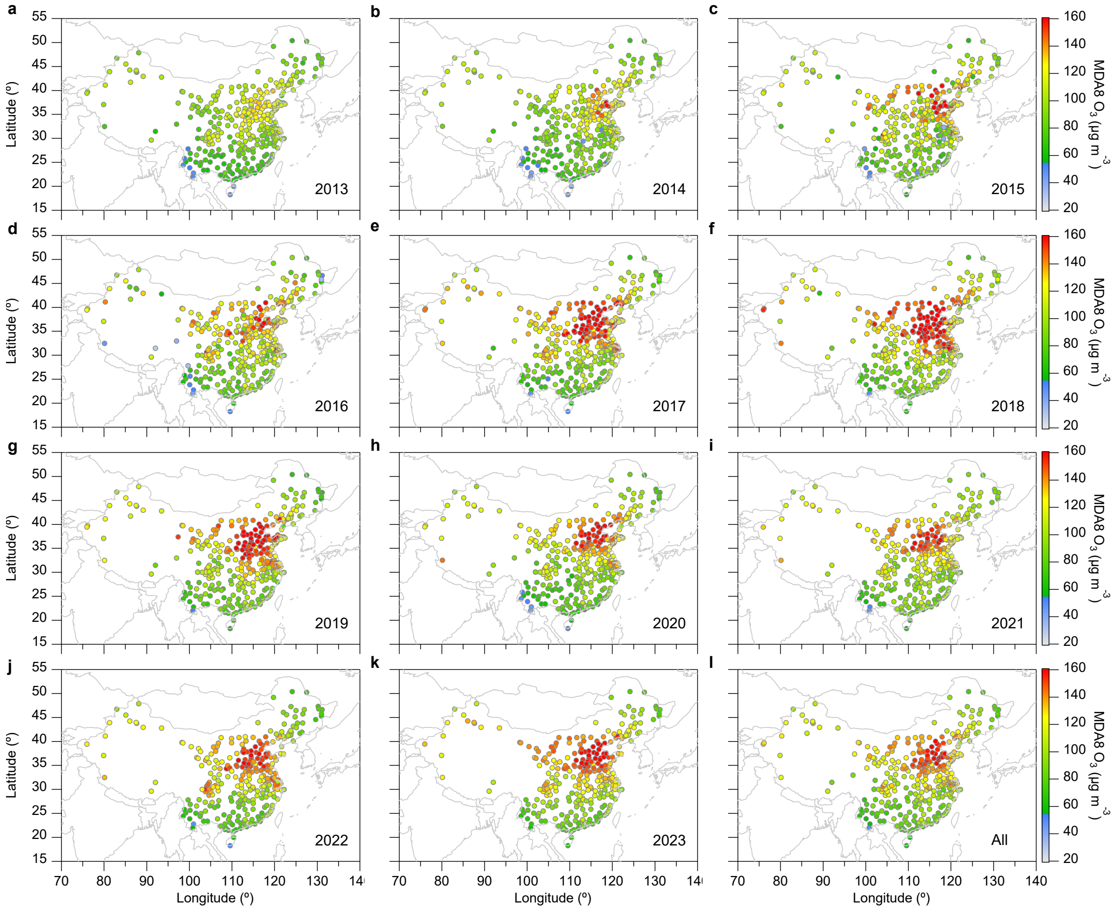


**Figure S1. Spatial distribution of MDA8 ozone from 2013 to 2023. a-f** display the mass concentrations of MDA8 ozone in 354 cities across China during the summertime months (June-July-August) from 2013 to 2023. **l** illustrates the average MDA8 ozone concentration over the 11-year period.

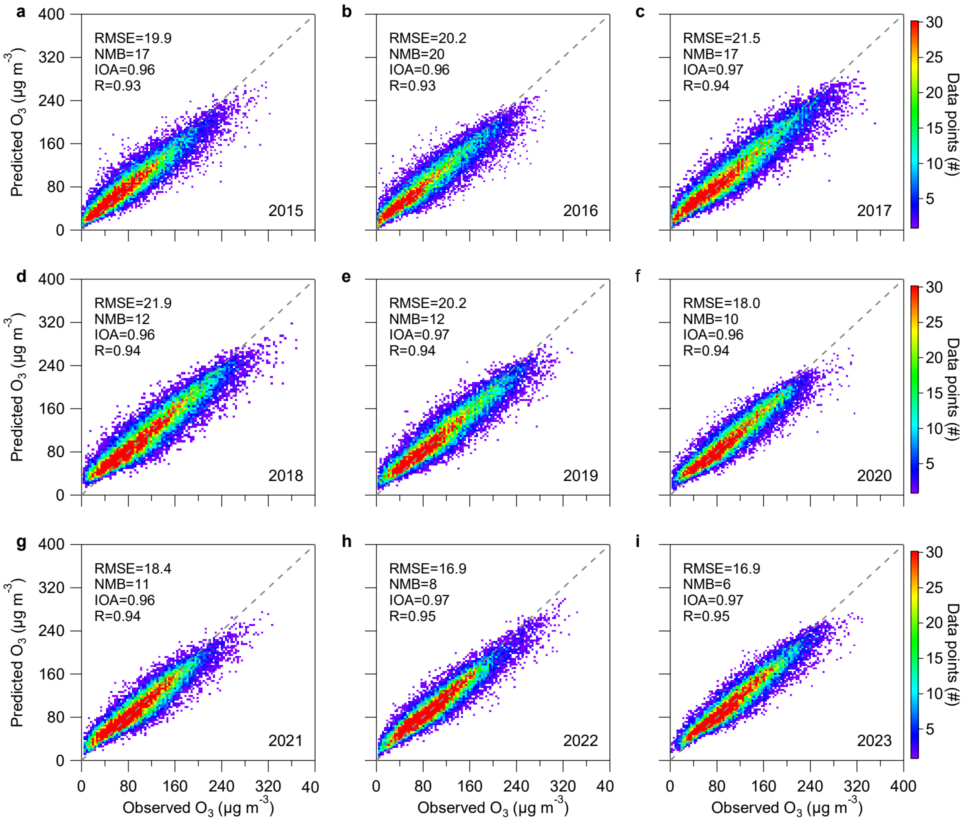


**Figure S2. Model performance evaluation.** Results of ten-fold cross-validation comparing observed and predicted values of the RF models for each year from 2015 to 2023 in the BTH region, using this region as an example.

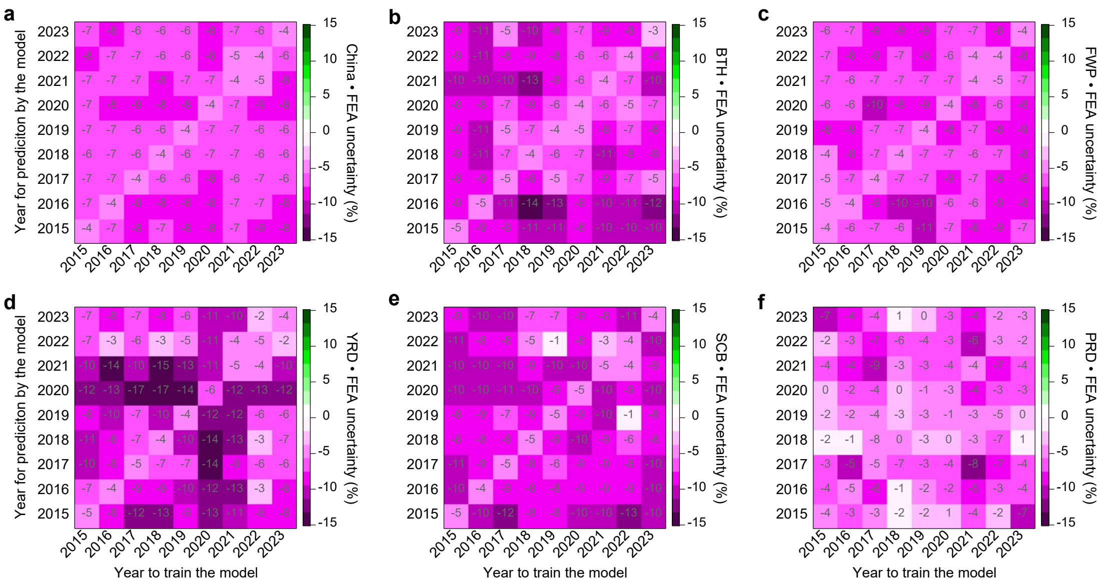


**Figure S3. Uncertainty of the FEA method without time variables.** The uncertainty for the FEA method is calculated using the approach described in Text S2. The x-axis represents the years used for model training, and the y-axis represents the years predicted by the trained model.The diagonal line in each sub-panel represents the changes in the residuals of the models.

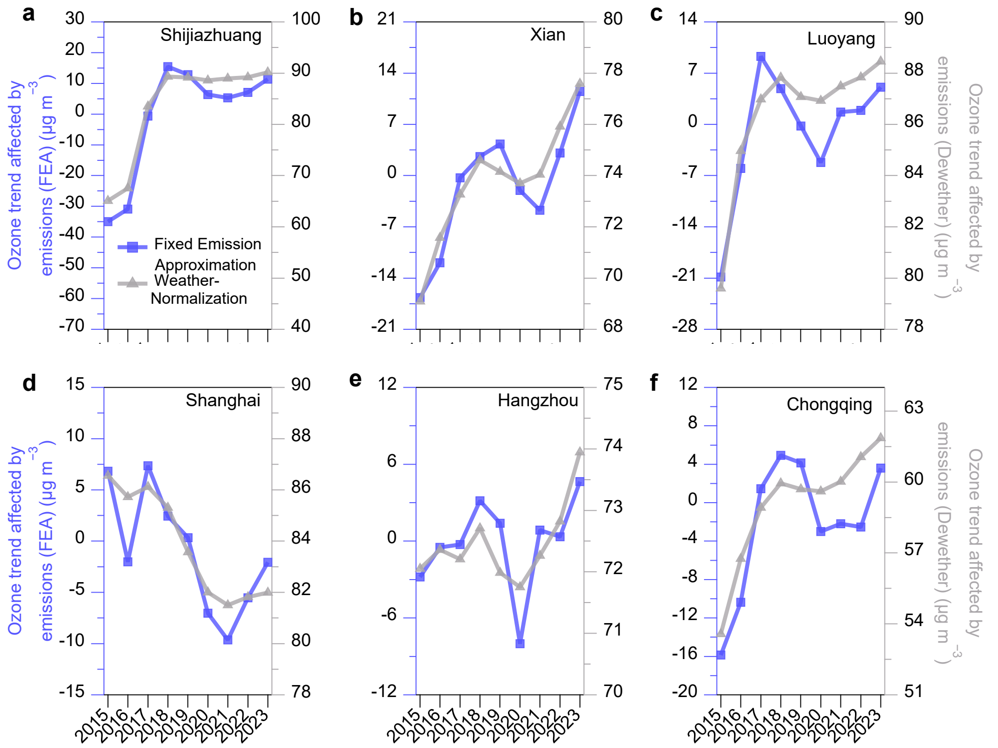


**Figure S4. Trends in the average summertime ozone concentration changes from 2015 to 2023, driven by anthropogenic emission control.** Panels compares the ozone trend variations for six representative cities in key regions, based on both the FEA method and the weather normalization method.

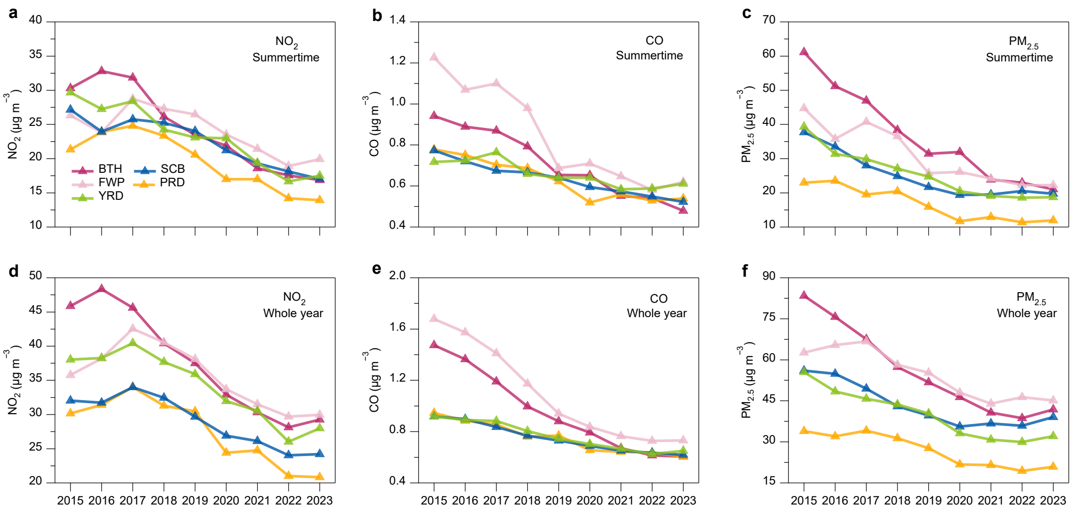


**Figure S5. Ground-based observed time series of $NO_2$, CO, and $PM_{2.5}$. a-c** show the summertime average time series of $NO_2$, CO, and $PM_{2.5}$ for China's five major city clusters regions from 2015 to 2023. **e-f** present the annual average time series of $NO_2$, CO, and $PM_{2.5}$ for China's five major city clusters regions from 2015 to 2023.

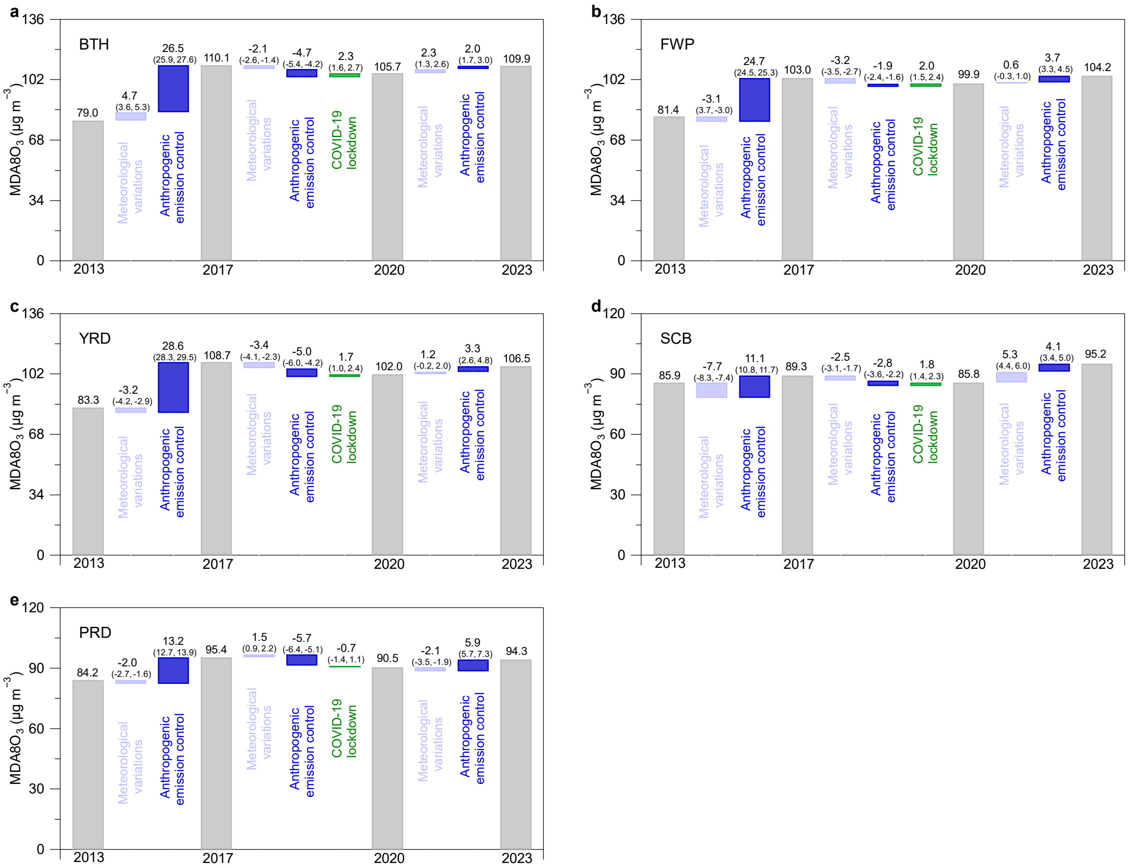


**Figure S6. Driving factors of MDA8 ozone from 2013 to 2023.** Changes in annual MDA8 ozone concentrations were decomposed into contributions from anthropogenic emissions, meteorological variability , and the COVID-19 lockdown using the FEA framework. Results reflect ensemble estimates based on multiple baseline years (2015–2023) for emissions. The interquartile range, with values in parentheses denoting the 25th and 75th percentiles across all baseline scenarios.

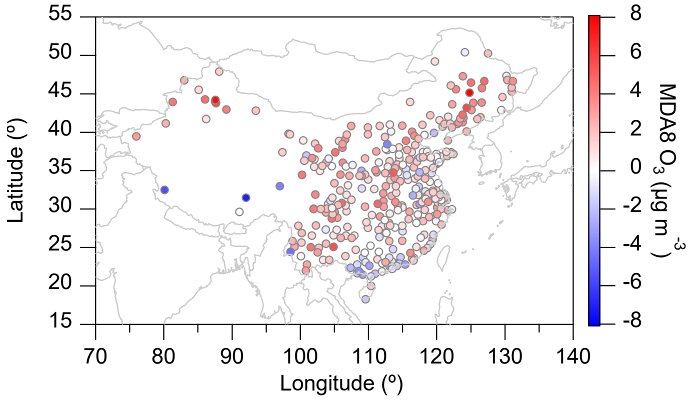


**Figure S7. Distribution of the relative contribution of the COVID-19 lockdown to MDA8 ozone in Chinese cities.** The quantified results in the figure were derived using the formula in Text S3.

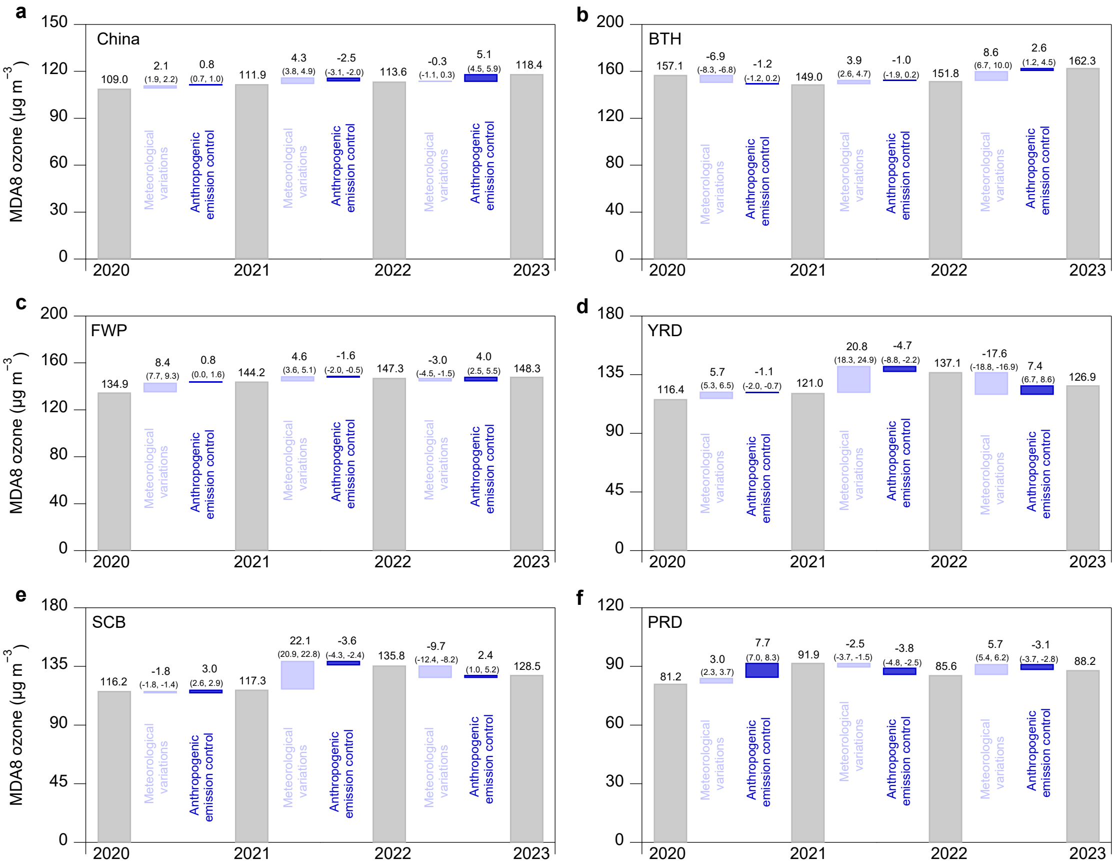

**Figure S8. Anthropogenic and meteorological drivers of ozone trends from 2020 to 2023.** Changes in summertime MDA8 ozone concentrations were decomposed into contributions from anthropogenic emissions and meteorological variability using the FEA framework. Results reflect ensemble estimates based on multiple baseline years (2015–2023) for emissions. The interquartile range, with values in parentheses denoting the 25th and 75th percentiles across all baseline scenarios.

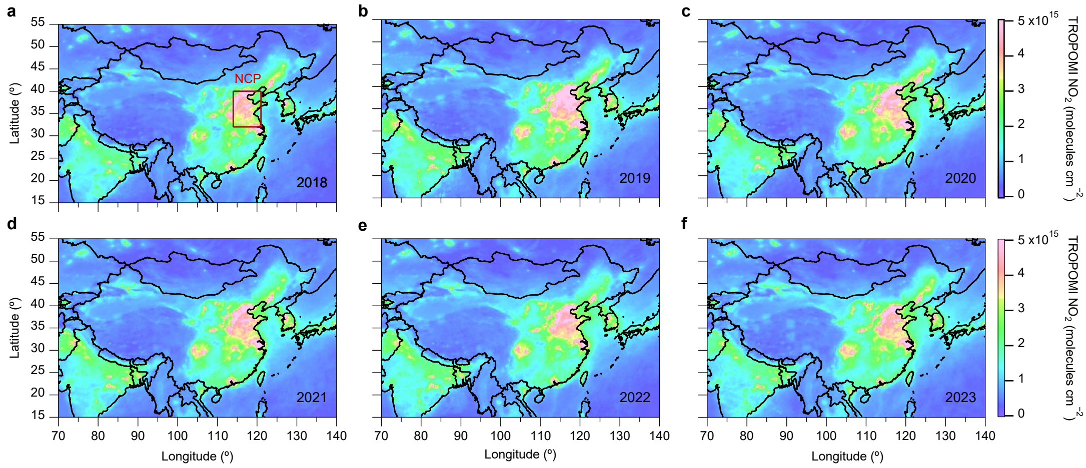


**Figure S9. Spatial and temporal variations of satellite $NO_2$.** Map of average levels of satellite-observed $NO_2$ from June-August 2018 to 2023**.** The rectangle in panel (a) represents the extent of the North China Plain (NCP).

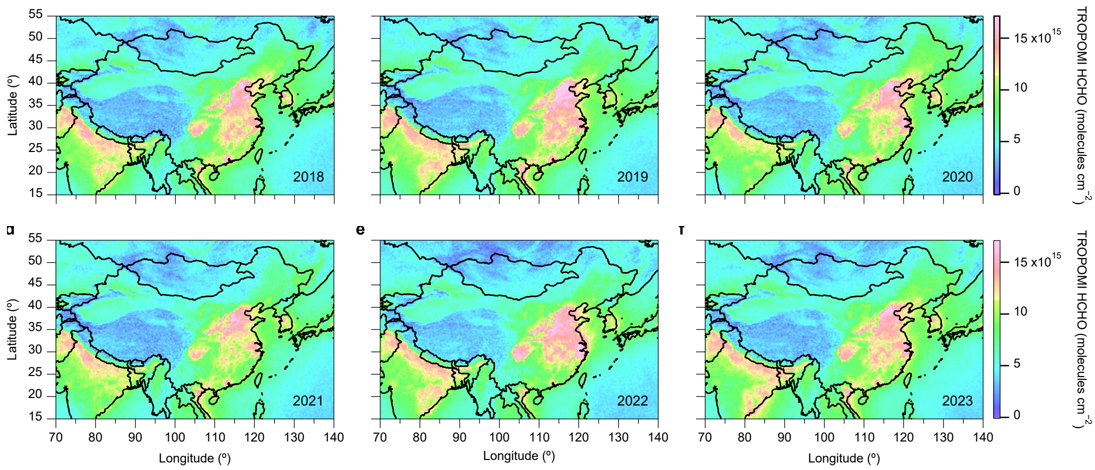


**Figure S10. Spatial and temporal variations of Satellite HCHO.** Map of average levels of satellite-observed HCHO from June-August 2018 to 2023.

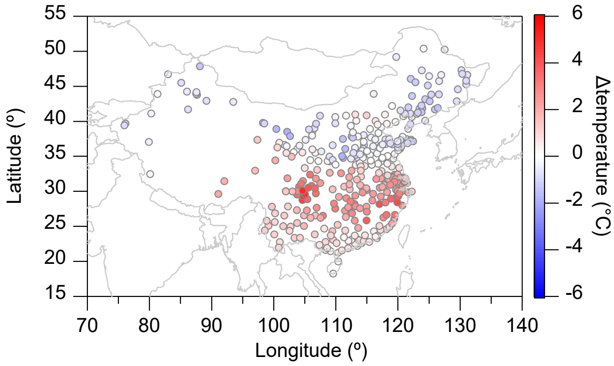


**Figure S11. Spatial distribution of daytime (11:00-17:00) temperature differences between HW and NHW.** The HW period is defined as July 16 to August 31, 2022, while the corresponding period in other years is considered as NHW.

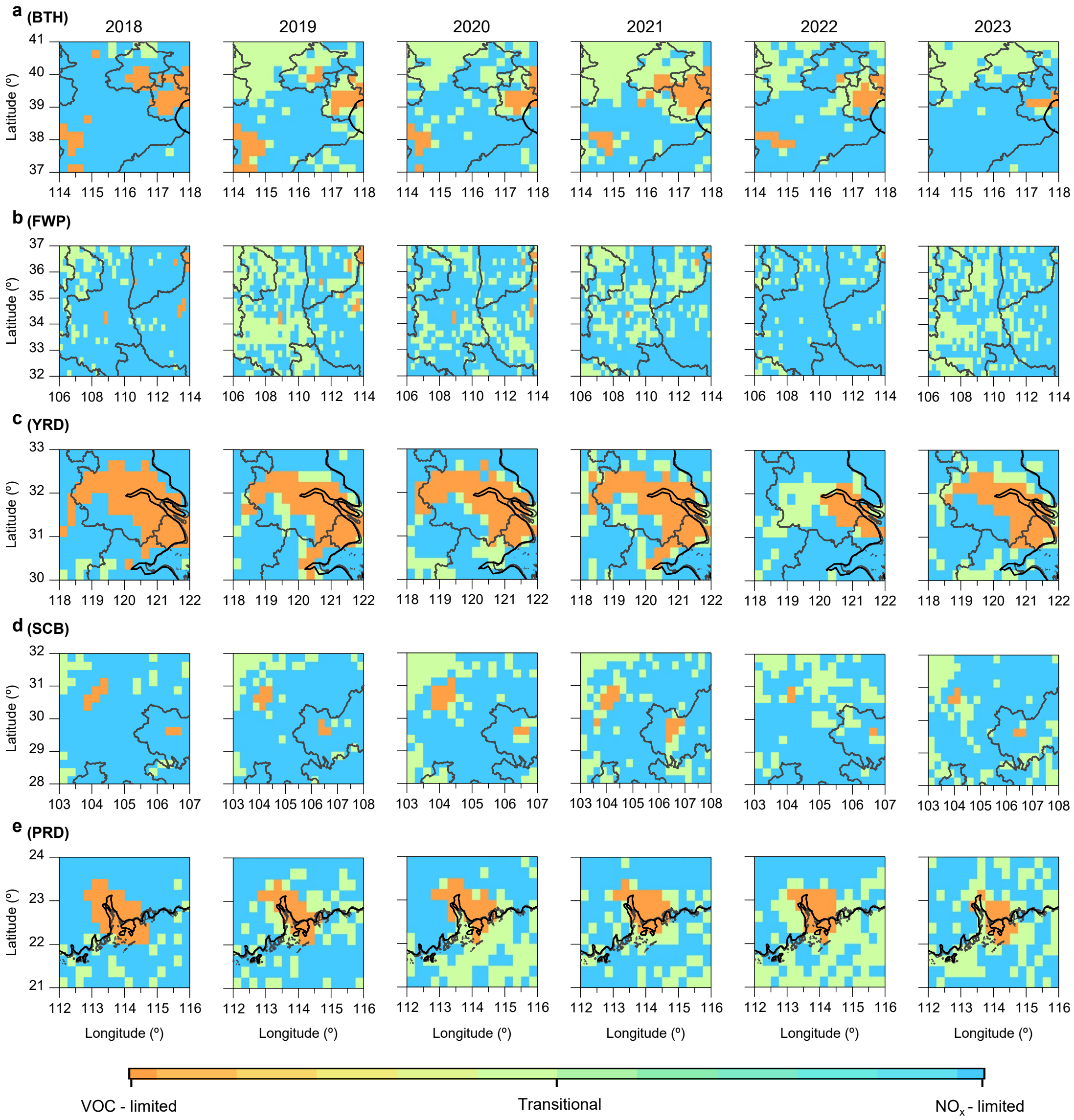


**Figure S12. Ozone formation sensitivity regimes.** The year-by-year results of FNR analysis from June to August (2018-2023) are presented, showing the spatiotemporal variation of ozone sensitivity in different regions. The colors in the map represent the geographical distribution of VOC-limited, $NO_x$-limited, and transitional ozone sensitivity regimes.

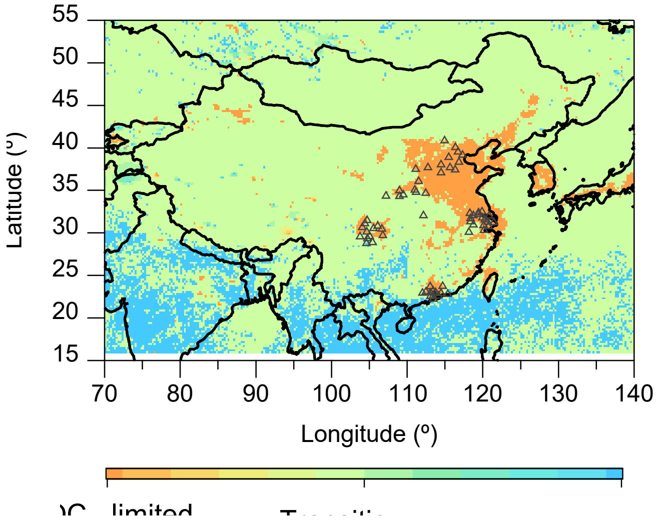


**Figure S13. Ozone formation sensitivity regimes during COVID-19.** Spatial distribution of ozone formation sensitivity regimes in China from January to April 2020 during the COVID-19 pandemic. The hollow triangles represent the geographical coordinates of five city cluster regions in China.

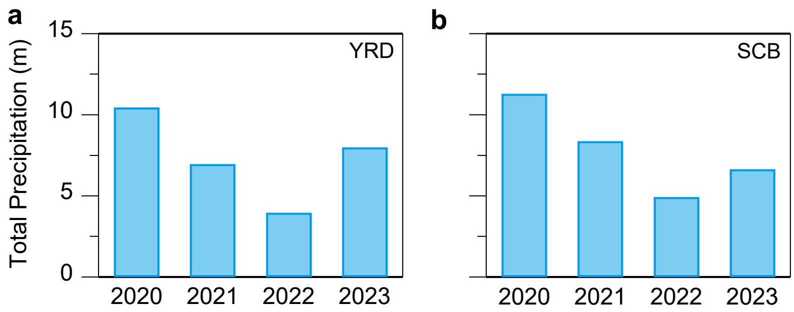


**Figure S14. Interannual variation in total precipitation.** Total precipitation in the SCB and YRD regions from June to August 2020 to 2023.

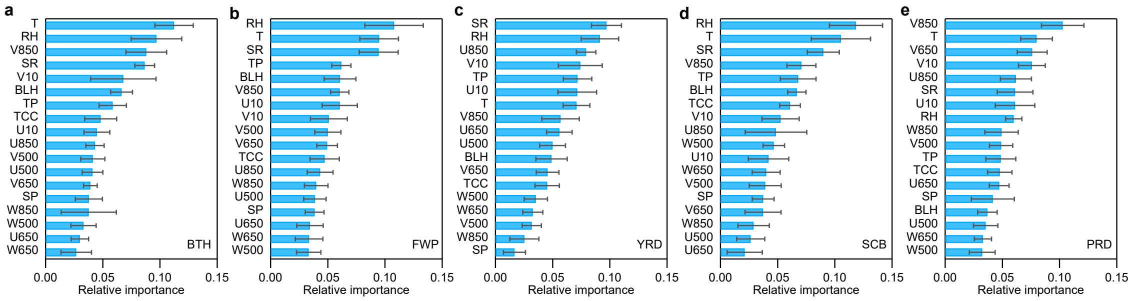


**Figure S15. Predicting the relative importance of characteristics.** The RF model has built-in importance (mean reduced impurity) for each predicted feature in each of the five typical regions.

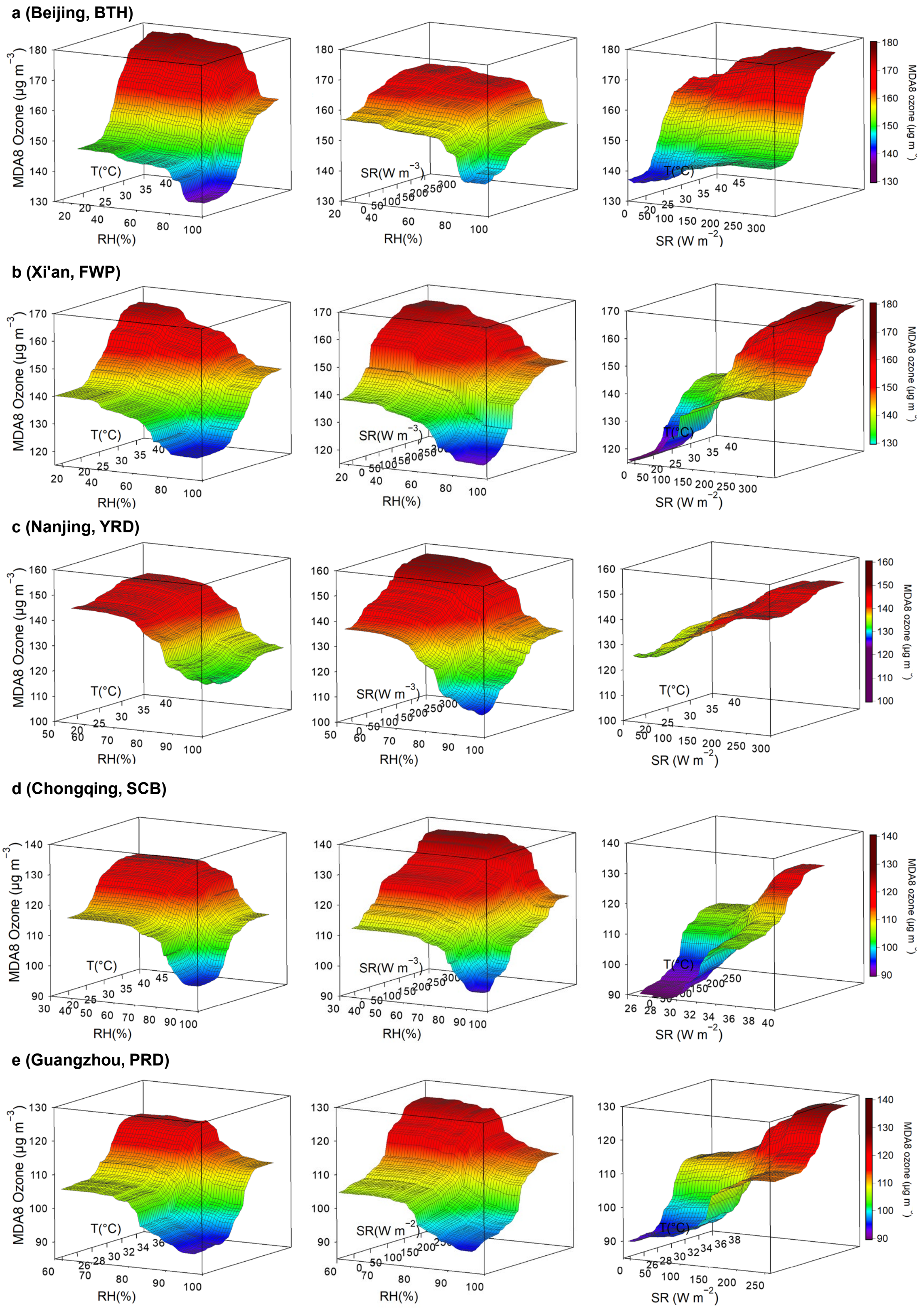


**Figure S16. Partial dependence of ozone on *T*, RH, and SR for representative cities.** Panels show the 3D-dependence plots of MDA8 ozone with RH, *T*, and SR for representative cities in BTH, FWP, YRD, and PRD, including MDA8 ozone-RH-*T*, MDA8 ozone-RH-SR, and MDA8 ozone-SR-*T*.

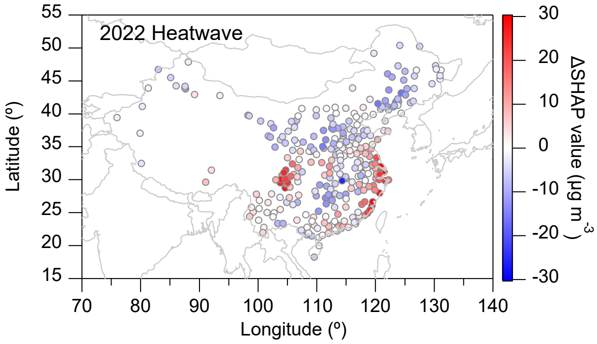


**Figure S17. Impact of the 2022 heatwave on MDA8 ozone.** Total relative contribution of meteorological conditions to MDA8 ozone during the 2022 heatwave period (from 16$^{th}$ July to 31$^{st}$ August).

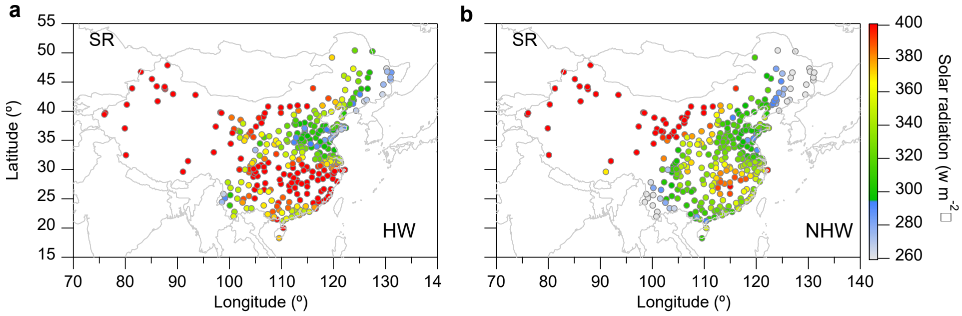


**Figure S18. Comparison of solar radiation between the HW and NHW periods.** Temporal and spatial distribution of daytime (10:00-17:00) mean solar radiation during the HW and NHW periods.

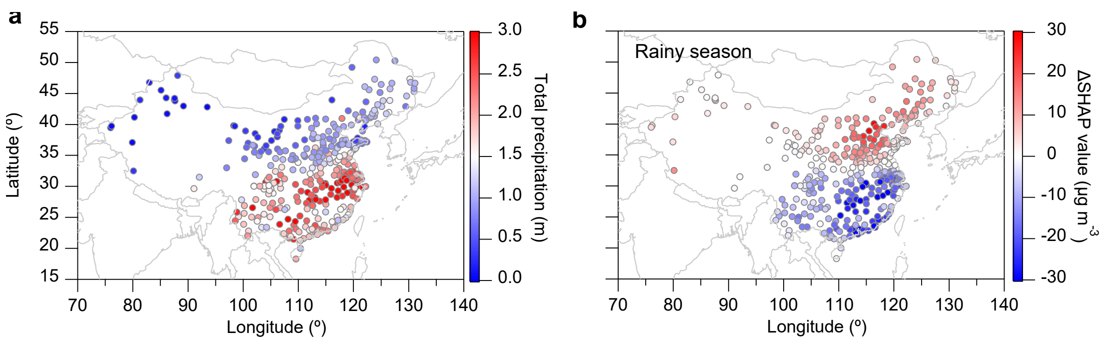


**Figure S19. Impact of the prolonged rainfall season on MDA8 ozone.** Total rainfall (a), and total relative contribution of meteorological conditions to MDA8 ozone (b) for 354 cities in China during the rainy season (from 15th June to 15th July) in the PR season during 2015-2023.

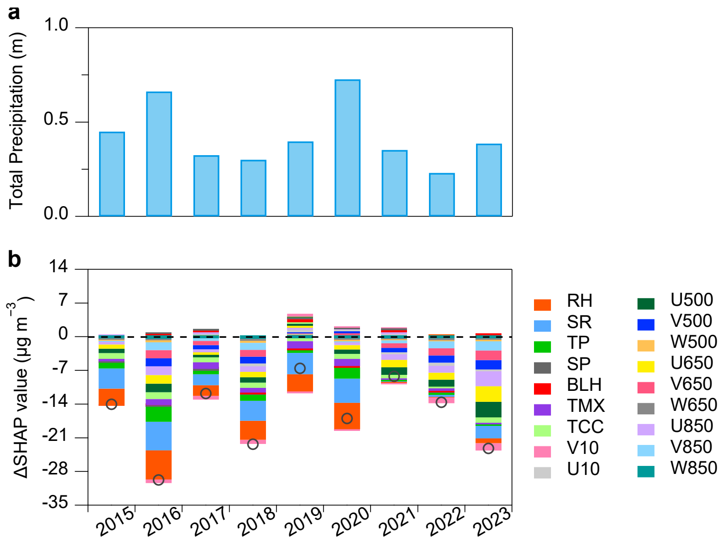


**Figure S20. Impact of the prolonged rainfall season on ozone concentrations. a** shows interannual variations in mean daily precipitation in the Yangtze-Huaihe region during the PR period. **b** presents relative contributions of meteorological conditions to MDA8 ozone from 2015 to 2023.

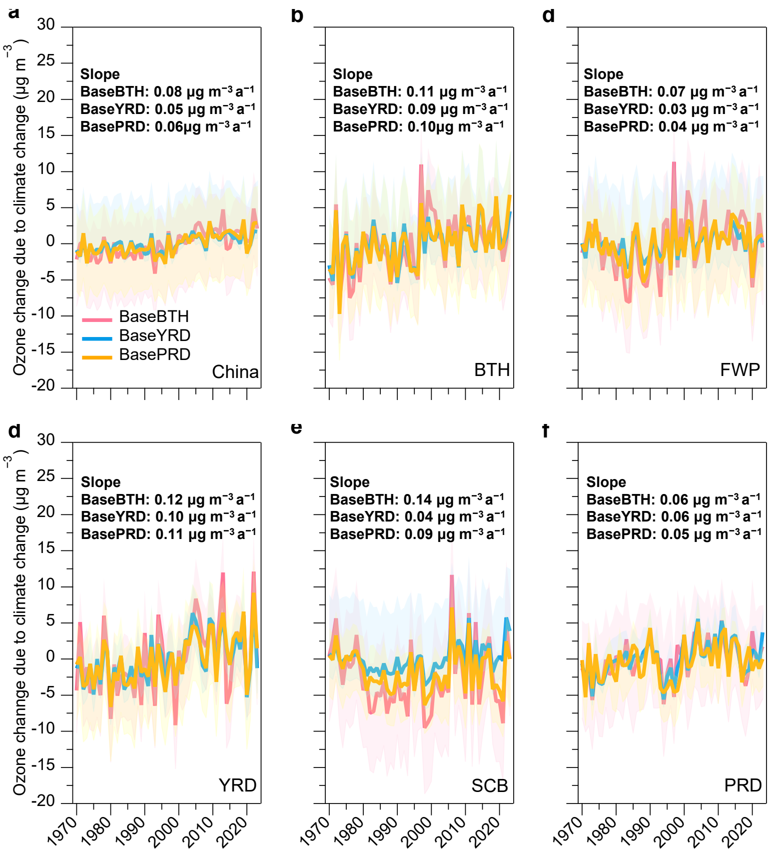


**Figure S21. Sensitivity simulation tests for different regions.** Three representative regional scenarios based on the characteristics of ozone pollution in China: the high ozone pollution scenario for BTH (BaseBTH), the moderate ozone pollution scenario for YRD (BaseYRD), and the low ozone pollution scenario for PRD (BasePRD). The figure evaluates trends in ozone pollution and climate impacts under different fixed anthropogenic emissions and atmospheric oxidative states.

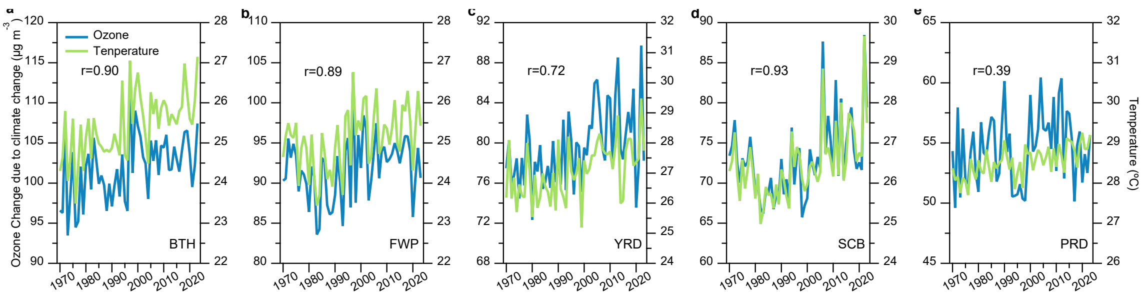


**Figure S22. Correlation between summertime ozone and mean surface temperature.** Changes in mean surface temperature and changes in mean ozone concentration driven by climate change over the period 1970 to 2023 (June-August). Correlation coefficients (r) between ozone and mean surface temperature for different regions are given in each panel.

**References**

Geng, G., Liu, Y., Liu, Y., Liu, S., Cheng, J., Yan, L., Wu, N., Hu, H., Tong, D., Zheng, B., Yin, Z., He, K., Zhang, Q.: Efficacy of China's clean air actions to tackle $PM_{2.5}$ pollution between 2013 and 2020, Nat. Geosci., 17, 987-994, https://doi.org/10.1038/s41561-024-01540-z, 2024.

Jin, X., Fiore, A., Boersma, K.F., Smedt, I.D., Valin, L.: Inferring changes in summertime surface ozone–$NO_x$–VOC chemistry over U.S. urban areas from two decades of satellite and ground-based observations, Environ. Sci. Technol., 54, 6518-6529, https://doi.org/10.1021/acs.est.9b07785, 2020.

Jin, X., Holloway, T.: Spatial and temporal variability of ozone sensitivity over China observed from the Ozone Monitoring Instrument, J. Geophys. Res. Atmos., 120, 7229-7246, https://doi.org/10.1002/2015JD023250, 2015.

Ren, J., Guo, F., Xie, S.: Diagnosing ozone–$NO_x$–VOC sensitivity and revealing causes of ozone increases in China based on 2013–2021 satellite retrievals, Atmos. Chem. Phys., 22, 15035-15047, https://doi.org/ 10.5194/acp-22-15035-2022, 2022.

Sillman, S.: The use of $NO_y$, $H_2O_2$, and $HNO_3$ as indicators for ozone-$NO_x$-hydrocarbon sensitivity in urban locations, J. Geophys. Res., 100, 14175-14188, https://doi.org/10.1029/94JD02953, 1995.

Wang, W., van der A, R., Ding, J., van Weele, M., Cheng, T.: Spatial and temporal changes of the ozone sensitivity in China based on satellite and ground-based observations, Atmos. Chem. Phys., 21, 7253-7269, https://doi.org/10.5194/acp-21-7253-2021, 2021.